ACS APPLIED MATERIALS & INTERFACES

Research Article

www.acsami.org

Self-Template Synthesis of Porous Perovskite Titanate Solid and Hollow Submicrospheres for Photocatalytic Oxygen Evolution and Mesoscopic Solar Cells

Jia Hong Pan,[†] Chao Shen,[†] Irina Ivanova,[‡] Na Zhou,[§] Xingzhu Wang,[†] Wee Chong Tan,[†] Qing-Hua Xu,[§] Detlef W. Bahnemann,[‡,∥] and Qing Wang*[,†]

[†]Department of Materials Science and Engineering, Faculty of Engineering, NUSNNI-NanoCore, National University of Singapore, 5 Engineering Drive 2, 117576 Singapore

[‡]Institut für Technische Chemie, Gottfried Wilhelm Leibniz Universität Hannover, Callinstraβe 3, D-30167 Hannover, Germany

[§]Department of Chemistry, National University of Singapore, 3 Science Drive 3, 117543 Singapore

[∥]Laboratory "Photoactive Nanocomposite Materials", Saint Petersburg State University, Ulyanovskaya Street 1, Peterhof, Saint Petersburg 198504, Russia

Supporting Information

ABSTRACT: We describe a general synthesis strategy, which combines sol–gel and hydrothermal processes, for the large-scale synthesis of porous perovskite titanates spheres with tunable particle size and inner structures. Amorphous hydrous TiO_2 solid spheres (AHTSS) are first synthesized by a sol–gel method and are then used as precursor and template for the subsequent hydrothermal reaction with alkaline earth metal ions in an alkaline medium. This strategy can be generalized to synthesize porous spheres of various perovskite titanates (i.e., $SrTiO_3$, $BaTiO_3$, and $CaTiO_3$) consisting of single-crystalline nanocubes. By controlling the textural properties (i.e., size, porosity, and structure) of AHTSS, perovskite titanates with tunable size and inner structures are selectively synthesized. The underlying formation mechanism is manifested by XRD and TEM to involve in situ crystallization or Ostwald ripening during the hydrothermal process. The obtained porous $SrTiO_3$ spheres present superior performance in photocatalytic oxygen evolution and CdSe-sensitized mesoscopic solar cells.

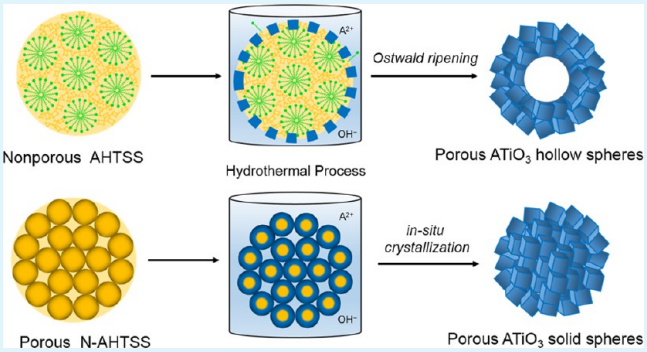

KEYWORDS: *perovskite titanate, TiO_2, photocatalysis, quantum dot sensitized solar cells, hollow spheres*

1. INTRODUCTION

Photoelectrochemical processes have proven to be cost-effective pathways for the efficient conversion of solar power to chemical and electrical energy, for which mesoscopic metal oxide semiconductors generally present as the key materials for light harnessing, charge transport, or both.[1,2] Among various semiconducting metal oxide nanostructures reported to date, monodisperse spheres comprised of nanocrystallites have been attracting particular interest. One of the most favorable features of these materials is the great structural diversity at nano- and submicrometer length scales, rendering unique textural properties: porous microstructure and large surface area arising from the voids among the assembled nanocrystallites, spherical morphology capable of enhancing the structural stability, ease of packing, processing, reclaiming, and so on. Taking TiO_2 as an example, recent studies have demonstrated that porous TiO_2 submicrospheres, as compared to the conventional nanoparticles (NPs), possess a larger surface area for dye uptake and present a significant size effect in light scattering. Moreover, their interconnected nanocrystalline network effectively shortens the diffusion path of charge carriers and decreases the resistances from the grain boundaries, both of which dramatically facilitate charge transport.[3−6] Therefore, superior performances in photocatalysis and mesoscopic solar cells have been achieved.[5,7−10]

Perovskite titanates ($ATiO_3$, A = alkaline earth metal) represent a unique class of oxides with intriguing properties in ferroelectricity, semi/superconductivity, catalysis, magnetism, and so on.[11−14] In particular, $SrTiO_3$ is a well-known n-type semiconductor widely used as photocatalysts and photoanode materials for mesoscopic solar cells.[15−22] Owing to the technical importance of $ATiO_3$, continuous efforts have been devoted to the facile and controlled synthesis of various nanostructured $ATiO_3$. Considerable progress has been made

Received: April 19, 2015
Accepted: June 19, 2015
Published: June 19, 2015

DOI: 10.1021/acsami.5b03396
ACS Appl. Mater. Interfaces 2015, 7, 14859−14869

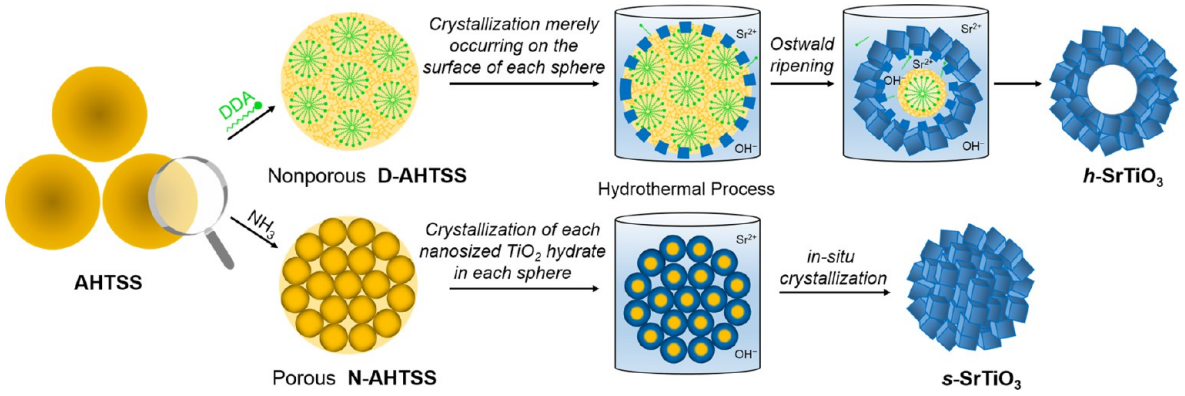

Figure 1. Schematic representation of the formation of amorphous hydrous TiO_2 solid spheres (D-/N-AHTSS), using DDA and NH_3 as the SDA, and their transitions to porous $SrTiO_3$ solid and hollow spheres (h-/s-$SrTiO_3$) via hydrothermal processes, respectively.

recently using wet-chemistry routes, and extensive success has been achieved in the synthesis of $ATiO_3$ NPs.[22−27] Compared with the traditional solid-state synthesis at a high temperature (>1000 °C), wet-chemistry routes, such as a one-pot hydro/solvothermal process, are favorable to reducing the crystal defects and coarsening at relatively low temperature.[16,28−34]

Despite the superior performance of porous spheres to NPs, self-organization of nano $ATiO_3$ to a well-defined porous spherical morphology appears to be a challenge. A key dilemma in the controllable synthesis lies in the comprehensive balance between the crystallization and the spherical assembly process.[5,35] The as-formed $ATiO_3$ nanocrystallites are prone to isolate from the highly curved spherical surface because of the increased stress, which easily causes the collapse of the spherical structure forming free NPs. Such destruction is even more severe during the fabrication of hollow spheres. Therefore, according to the protocols established so far, the synthesized $ATiO_3$ (sub)microspheres generally present low porosity and limited surface area (<20 m^2 g^{-1}),[29,36,37] which significantly restrict their practical applications. Moreover, on the basis of our careful literature survey, size- and inner-structure-controllable synthesis of spherical $ATiO_3$ has not yet been reported.

In an effort to develop a facile synthesis method for porous $ATiO_3$ solid/hollow submicrospheres with large surface areas and tunable particle sizes, we consider decoupling the formation of the spherical structure from the crystallization process. Thereby, $ATiO_3$ can be incubated in the mother spherical structure, alleviating the control of crystal growth and favoring the retention of the spherical morphology.[5,38−41] In this context, amorphous hydrous TiO_2 solid submicrospheres (AHTSS) would be an appropriate "self-template" because we have recently studied these for the size-controllable synthesis of mesoporous TiO_2 solid/hollow submicrospheres.[38,40] More significantly, compared with anatase or rutile TiO_2, amorphous TiO_2 has been demonstrated to be an ideal precursor that enables the transformation to nanocrystalline $ATiO_3$ at a relatively low hydrothermal temperature, as investigated by Walton et al.[42] The decreases in reaction temperature and pressure allow the $ATiO_3$ nanocrystallites to be incubated and to ripengradually, which in turn facilitates the retention of spherical and hollow structures. Therefore, we propose a combined sol−gel and low-temperature hydrothermal process for the large-scale synthesis of a series of porous and spherical $ATiO_3$ (A = Sr, Ba, and Ca) with tunable inner structure and particle size. Figure 1 illustrates the formation of porous $SrTiO_3$ solid and hollow submicrospheres (s-/h-$SrTiO_3$, respectively) using AHTSS as the self-template. AHTSS are first formed by the sol−gel precipitation of titanium alkoxides. The subsequent hydrothermal reaction with alkaline earth metal ions proceeding in an alkaline medium leads to a phase transformation from AHTSS to $ATiO_3$ with the spherical structure inherited. On the basis of this synthesis strategy, the solid/hollow interior structure and the particle size of $ATiO_3$ submicrospheres can be selectively controlled by tuning two key textural parameters of AHTSS self-template, namely porosity and size. The as-synthesized porous $SrTiO_3$ submicrospheres, possessing a large surface area up to 95.6 m^2 g^{-1}, show excellent performance in photoelectrochemical applications.

2. EXPERIMENTAL SECTION

2.1. Chemicals. All chemicals used were obtained from Sigma-Aldrich and used as received without further purification, except titanium isopropoxide ($Ti(O\text{-}iPr)_4$, ≥97%) that was purified by distilling at 120 °C under reduced pressure. The obtained colorless and transparent liquid was used for the subseqent synthesis of AHTSS self-templates.

2.2. Synthesis of AHTSS with DDA (D-AHTSS). Typically, 1.08 g of dodecylamine (DDA) was readily dissolved in 200 mL of a mixture of ethanol and acetonitrile (3:1 in volume ratio) containing 1.15 g of H_2O. After stirring for 10 min, 4 mL of $Ti(O\text{-}iPr)_4$ was promptly injected under vigorous stirring. A milky suspension was formed in 2 s. After aging for 6 h by gentle stirring, the formed D-AHTSS were centrifuged, washed by ethanol once, and then washed by water three times. Finally, they were dried at 80 °C.

2.3. Synthesis of AHTSS with NH_3 (N-AHTSS). Typically, 0.38 g of $NH_3{\cdot}H_2O$ (28 wt %) solution and 0.91 g of H_2O were added to 250 mL of a mixture of ethanol and acetonitrile (6:4 in volume ratio). Then, 5 mL of $Ti(O\text{-}iPr)_4$ was promptly injected into the above solution under vigorous stirring. A milky suspension was formed in 2 s. After aging for 6 h by gentle stirring, the formed N-AHTSS were centrifuged, washed by ethanol once, and then washed by water three times. Finally, they were dried at 80 °C.

2.4. A General Synthesis Method of s-/h-$SrTiO_3$. Typically, 1.0 g of dried AHTSS was redispersed in 35 mL of 2 mol L^{-1} NaOH aqueous solution. $Sr(NO_3)_2$ was then added with a final molar ratio to TiO_2 of 1.1:1.0. After stirring for 10 min, the suspension was transferred to a 45 mL Teflon-lined autoclave. A hydrothermal reaction was carried out at 140 °C for 4 h to conduct the crystallization. The obtained white particles were collected, washed with 0.05 mol L^{-1} HNO_3 and water to remove the unreacted $Sr(OH)_2$, and finally calcined at 450 °C for 4 h with a ramping rate of 5 °C min^{-1}. By tuning the type of AHTSS, s-/h-$SrTiO_3$ can be selectively synthesized using N-/D-AHTSS, respectively.

DOI: 10.1021/acsami.5b03396
ACS Appl. Mater. Interfaces 2015, 7, 14859−14869

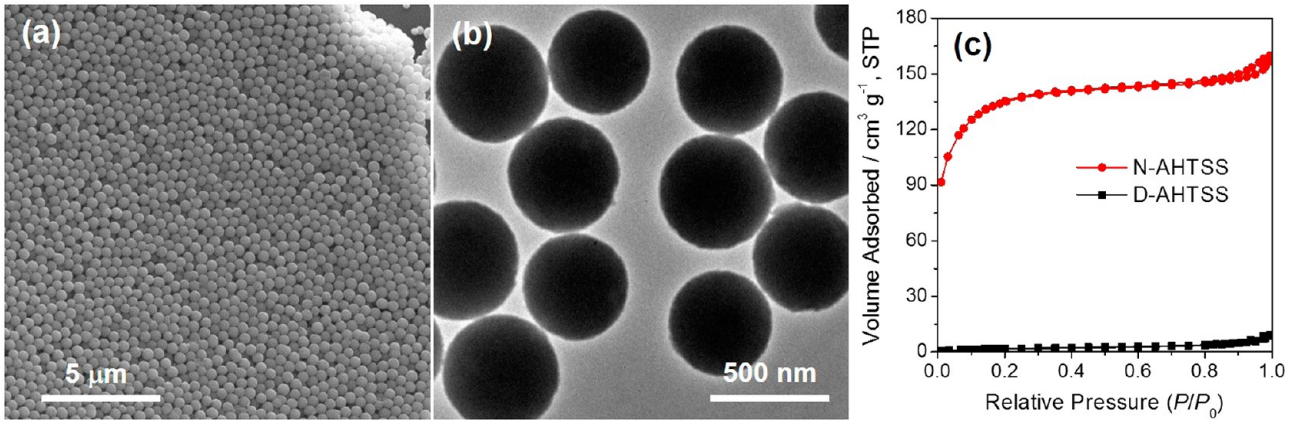

Figure 2. (a) TEM and (b) SEM images of D-AHTSS. (c) N_2 sorption isotherm plots of D-/N-AHTSS.

2.5. Materials Characterization. XRD patterns were collected on a Bruker D8 Advance X-ray diffractometer using monochromated high-intensity Cu Kα radiation with a wavelength of 0.15418 nm. The morphology and microstructure were characterized by a Zeiss Supra 40 field-effect scanning electron microscope (SEM) and a transmission electron microscope (TEM, JEOL JEM-2010). Nitrogen sorption isotherms were measured by an ASAP 2020 system (Micromeritics). The Brunauer–Emmett–Teller (BET) equation was used to calculate the surface area from the adsorption data obtained at P/P_0 = 0.01–0.30. The Barrett–Joyner–Halenda (BJH) method was used to estimate the average pore diameter from the adsorption branch of the isotherm. TGA was performed in air with a heating rate of 10 °C min^{-1} using a SDT Q600 V8.0 Build 95 thermoanalytical apparatus. The optical properties of $SrTiO_3$ powders and $SrTiO_3/TiO_2$ electrodes were studied utilizing a single beam in a Shimadzu UV–vis–NIR spectrophotometer (Solidspec-3700).

2.6. Photocatalytic Activity Measurements. Photocatalytic oxygen evolution tests were conducted in a continuous-flow setup adapted to a quadrupole mass spectrometer (QMS) for the gas analysis (Hiden HPR-20). The experimental setup employed in this study was the same as that described in our previous report.[43] In a typical run, the $SrTiO_3$ (1.0 g L^{-1}) photocatalyst was suspended in 50 mL of an aqueous $AgNO_3$ solution (0.01 mol L^{-1}) by sonication. The suspension was transferred into the photoreactor and purged with Ar for 30 min to sufficiently remove dissolved O_2. Afterward, the reactor was connected to the mass flow controller and to the Q/C capillary sampling inlet of the QMS through metal flanges and adapters. To remove the air in the headspace of the reactor, an Ar gas stream was allowed to flow continuously through the reactor before irradiation, until no traces of molecular oxygen or nitrogen could be detected by the QMS. The Ar gas flow rate through the reactor was kept constant at 10 mL min^{-1} during all photocatalytic tests. The inlet flow rate/gas consumption by the QMS was 1 cm^3 min^{-1}, and the excess gas was directed toward the exhaust. The sampling rate of the QMS was in the millisecond time range, thus allowing fast tracking of the reaction. After stabilization of the system background, the reactor was irradiated from the outside using collimated UV light of a strong 365 nm LED (Thorlabs). For the quantitative analysis of O_2, the QMS was calibrated employing standard diluted O_2 in Ar (Linde Gas, Germany).

2.7. Fabrication of Mesoscopic Solar Cells. Viscous pastes of commercial Evonik-Degussa Aeroxide P25 TiO_2 NPs and *s*-/*h*-$SrTiO_3$ were made by mixing with ethyl cellulose and α-terpineol following our previously reported procedure.[38,44] The prepared P25 paste was first screen-printed onto fluorine-doped tin oxide (FTO)-coated glass (15 Ω sq^{-1}, Pilkington TEC-15) that was predeposited with a thin compact TiO_2 layer by spray pyrolysis. Then, the transparent P25 layer was deposited with a scattering layer by screen-printing the $SrTiO_3$ paste. The resultant films were calcined in air at 450 °C for 15 min before being subjected to a diluted $TiCl_4$ solution, rinsed, dried, and heated to 450 °C again for 30 min.

The fabricated photoanodes were sensitized with CdSe by successive ionic layer adsorption and reaction (SILAR) method by dipping into two separated solutions containing 0.03 mol L^{-1} cadmium nitrate tetrahydrate (Fluka, >99.0%) and 0.03 mol L^{-1} Se^{2-}.[44−47] The Se^{2-} solution was prepared by mixing SeO_2 and $NaBH_4$ in ethanol following a procedure developed by Lee et al.[48] The desired CdSe clusters were formed by the reaction of the preadsorbed Cd^{2+} with Se^{2-}. One deposition cycle was completed by further rinsing in ethanol for 2 min and drying again in an argon atmosphere for 2 min. This procedure was repeated nine times. The obtained CdSe-loaded TiO_2 electrodes were then deposited with a ZnS passivation layer using 0.1 mol L^{-1} aqueous zinc acetate dehydrate ($Zn(CH_3COO)_2{\cdot}2H_2O$) and 0.1 mol L^{-1} aqueous sodium sulfide nonahydrate ($Na_2S{\cdot}9H_2O$), dipping for 1 min in each solution, with 1 min of rinsing in deionized water between each immersion in a precursor solution. After two deposition cycles, a core–shell CdSe/ZnS sensitizer layer was formed on photoanodes.

For the construction of solar cell, an aqueous polysulfide solution composed of 1.0 mol L^{-1} $Na_2S{\cdot}9H_2O$, 1.0 mol L^{-1} S, and 0.10 mol L^{-1} NaOH was used as the electrolyte for CdSe-sensitized solar cell, and FTO with a thin Pt layer was used as the counter electrode. Alternatively, a Cu_2S counter electrode prepared by adding one drop of the polysulfide solution onto an unmasked part of well-etched brass was used.[45]

2.8. Characterization of Mesoscopic Solar Cells. Photocurrent–voltage (j–V) characteristics were measured under simulated AM 1.5G illumination using a Keithley Source Meter and the PVIV software package (Newport). A Newport solar simulator was used as a light source, and its light intensity was calibrated using a reference Si solar cell (Model: 91150V, Newport/Oriel). The active area of the cells was defined by a black mask to be 0.1199 cm^2. Incident photon conversion efficiency (IPCE) spectra were measured under short-circuit condition in air using a 300 W xenon lamp and a grating monochromator equipped with order sorting filters (Newport/Oriel). The spectral resolution was set to 5 nm. The incident photon flux was determined by using a calibrated silicon photodiode. Photocurrents were measured with an autoranging current amplifier. Control of the monochromator and recording of the photocurrent spectra were carried out via the TRACQ Basic software (Newport).

3. RESULTS AND DISCUSSION

3.1. Synthesis of AHTSS with Controllable Textural Properties. The AHTSS were synthesized by direct hydrolysis of Ti(O-iPr)$_4$ in a mixed ethanol–acetonitrile solution with small amounts of water and structure-directing agent (SDA). Acetonitrile is used as a cosolvent to improve the monodispersity of the resultant AHTSS.[5] The SDA, either DDA or NH_3, is used as spherical morphology controller and precipitation prompter for the rapid hydrolysis of Ti(O-iPr)$_4$,

DOI: 10.1021/acsami.5b03396
ACS Appl. Mater. Interfaces 2015, 7, 14859–14869

which generates ultrafine $Ti(O\text{-}iPr)_x(OH)_{4-x}$ NPs. Moreover, with the assistance of SDA, these NPs serve as nucleation centers for the subsequent agglomeration of the nanosized hydrates. Uniform and monodisperse solid spheres can thus be formed via self-organization.[49]

Apparently, the particle size of AHTSS is critically determined by the quantity of nucleation centers created by water. Tuning the molar ratio of H_2O to $Ti(O\text{-}iPr)_4$ (R_H) from 2.5 to 15 enables the formation of monodispersed AHTSS with particle sizes in range of 0.2−1.1 μm (see Figure S1 and ref 38.). The higher R_H is, the more nucleation centers are formed, and consequently, the smaller the particle size will be.

DDA (or NH_3) mediates the self-organization of primary TiO_2 hydrates to AHTSS. These SDAs play unique roles in the formation of AHTSS. Tuning SDA allows for a facile control of their textural properties, e.g., their porosity. Figure 2a,b shows the representative SEM and TEM micrographs of D-AHTSS synthesized with an R_H of 4.7. They are solid and exhibit high uniformity in particle size (~480 nm). Similar uniform spherical morphology is also present in N-AHTSS, as can be found in our previous report.[38]

Nevertheless, there is a significant difference in their specific surface area, as revealed by N_2 adsorption analysis (Figure 2c). D-AHTSS has a nonporous structure with a limited BET surface area of 6.87 m^2/g, whereas N-AHTSS possesses an ultralarge surface area of 467.4 $m^2\ g^{-1}$ and a uniform BJH pore diameter of 3.5 nm. With DDA as SDA, an organic−inorganic hybrid mesostructure can be formed through a so-called S^0I^0 pathway by the cooperative assembly between the neutral DDA surfactants (S^0) and the inorganic precursor (I^0) of hydrophilic TiO_2 hydrates.[5,50−53] Through such cross-linking, DDA molecules are associated with TiO_2 hydrates in D-AHTSS. Thermogravimetric analysis (TGA) of D-AHTSS shows that the DDA/TiO_2 weight ratio is around 0.27. Similar to the mesostructured DDA-SiO_2 hybrid materials,[50] D-AHTSS show nonporous nature, and their surface area is mainly attributed to their surface roughness.[51,54] In comparison, because of the increasing OH^- with the introduction of NH_3 as SDA, hydrogen bonding and electrostatic attractions dominate the self-assembly, guiding the formation of N-AHTSS with the close packing of nanosized TiO_2 hydrates. Porous structure can thus be formed because of the existence of numerous voids among the TiO_2 hydrates.[38]

3.2. Hydrothermal Transformation from AHTSS to $ATiO_3$. The nanosized TiO_2 hydrates show a high reactivity with alkaline earth hydroxides during the hydrothermal process. A variety of prototypical ATiO3, including $SrTiO_3$, $BaTiO_3$, and $CaTiO_3$, can be synthesized at a moderate hydrothermal temperature of 140 °C. Herein, we take $SrTiO_3$ as an example to expound our synthesis strategy.

Figure 3 summaries the morphology and microstructure of *s*-/*h*-$SrTiO_3$ synthesized from N-/D-AHTSS. After a mild hydrothermal reaction followed by a calcination at 450 °C, *s*-/*h*-$SrTiO_3$ inherit the spherical morphology of their self-templates, although the diameter is decreased to 420−450 nm and the uniformity is slightly degraded because of the structural shrinkage caused by the crystallization of $SrTiO_3$. More interestingly, tuning the self-template allows for the facile synthesis of $SrTiO_3$ submicrospheres with controllable inner structures. For instance, *s*-$SrTiO_3$ derived from N-AHTSS possesses a solid interior and consists of numerous $SrTiO_3$ nanocubes, the typical crystal shape of perovskites (Figure 3a,b). The edge length of the packed $SrTiO_3$ nanocubes is very

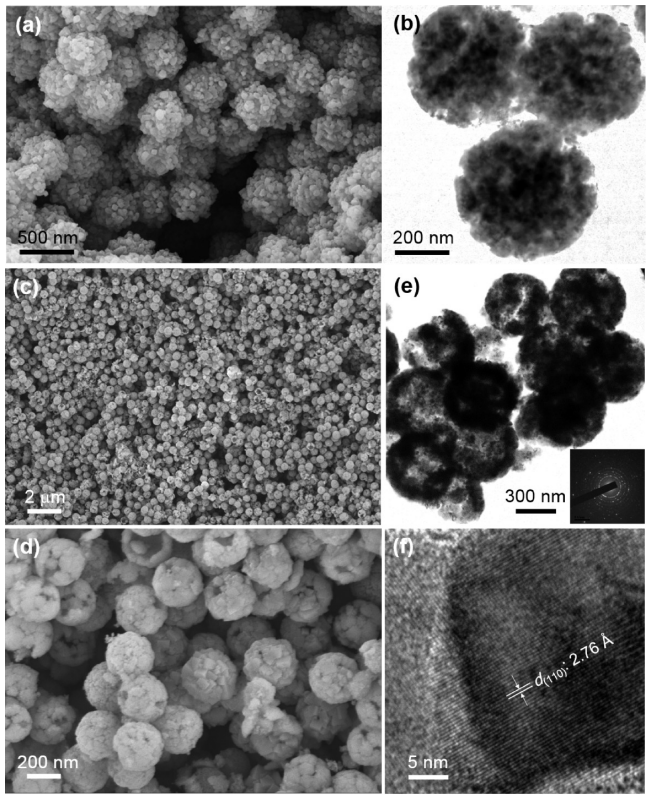

Figure 3. (a, c, and d) SEM , (b and e) TEM, and (f) HRTEM images of *s*-$SrTiO_3$ (a and b) and *h*-$SrTiO_3$ (c−f) synthesized from N-/D-AHTSS, respectively.

uniform and estimated to be around 30−40 nm. Voids among these nanocubes create accessible mesopores and channels inside the solid submicrospheres. In contrast, *h*-$SrTiO_3$ with a hollow interior is obtained when using D-AHTSS as self-template. The densely packed $SrTiO_3$ nanocubes construct a spherical shell with a thickness of 120−180 nm (Figure 3c−e). A high-resolution TEM (HRTEM) image shown in Figure 3f reveals that each nanocube is fully crystallized. The *d* spacing of the lattice fringes is calculated to be 2.76 Å, which can be assigned to the (110) surface of $SrTiO_3$.[55]

N_2 adsorption−desorption isotherms were measured for *s*-/*h*-$SrTiO_3$ after calcination at 450 °C to further elucidate their microstructure evolution upon phase transition. As shown in Figure 4, they exhibit type-IV isotherm plots with distinct capillary condensation steps, suggesting the presence of mesopores in both samples. BET specific surface areas of *s*-/*h*-$SrTiO_3$ are estimated to be 101.3 and 64.7 m^2g^{-1}, respectively. A type H3 hysteresis loop at P/P_0 = 0.6−1.0 is observed in *s*-$SrTiO_3$, which can be assigned to slit-shaped pores constructed by the packed nanocubes.[56,57] In contrast, *h*-$SrTiO_3$ exhibits two hysteresis loops in the sorption isotherm. At P/P_0 = 0.40−0.75, the hysteresis loop is of type H2, suggesting the presence of inkbottle-like pores arising from the intra-aggregated pores. At P/P_0 = 0.8−1.0, the hysteresis loop is of type H4, which is ascribed to the narrow slit-like pores because of the large interaggregated pores enriched by the generation of hollow interiors.[58] Accordingly, *h*-$SrTiO_3$ presents a bimodal pore size distribution ranging in the mesoporous and macroporous regions centered at 3.4 and >100 nm, respectively.

DOI: 10.1021/acsami.5b03396
ACS Appl. Mater. Interfaces 2015, 7, 14859−14869

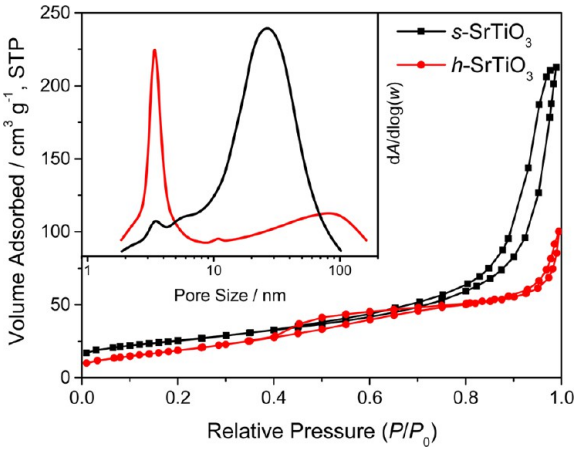

Figure 4. N_2 sorption isotherms and pore size distribution plots (inset) for *s*-/*h*-$SrTiO_3$.

It is worth noting that these two kinds of porous $SrTiO_3$ submicrospheres present much larger surface area than those obtained from the solid-state reaction or from the sol−gel coprecipitation method followed by calcination, where amorphous titanates directly crystallize into dense crystals inevitably eliminating their surface area.[28,59] In our synthesis strategy, $SrTiO_3$ building blocks are incubated under hydrothermal conditions, which facilitates the crystal growth of $SrTiO_3$ at the nanoscale. Hence, the hydrothermally prepared submicrospheres possess a large surface area, up to 170.2 m^2 g^{-1} (Figure S2), and show superior thermal stability resistance to indiscriminate crystal growth or fusion in the subsequent calcination process. As a result, a porous structure with a large surface area is obtained.

3.3. Formation Mechanism. The transformation from AHTSS to perovskite $SrTiO_3$ occurs during the hydrothermal process and is accompanied by substantial structural evolutions. The synthesis is derived from an aqueous NaOH solution containing suspended AHTSS and $Sr(OH)_2$. Herein, $Sr(OH)_2$ is freshly formed by mixing $Sr(NO_3)_2$ with NaOH. Its solubility in water can be dramatically increased at elevated temperature (e.g., 1.77 g per 100 mL at 20 °C, as compared with 21.83 g per 100 mL at 100 °C). Hence, the formed $Sr(OH)_2$ precipitate can be readily dissolved in the aqueous medium at the hydrothermal temperature 140 °C. Therefore, the formation of $SrTiO_3$ is believed to occur at the solid (AHTSS)−liquid (Sr^{2+}-containing alkaline solution) interface, ensuring uniform morphology and easy crystallization.

The intermediates at different stages of hydrothermal reaction were collected, and their structure and morphology were analyzed. Figure 5a shows the XRD patterns of D-AHTSS after hydrothermal reaction durations of 0.5, 1.5, 3, and 4 h. All four samples display only one SrTiO3 phase (Powder Diffraction File (PDF) no. 73-0661, International Centre for Diffraction Data (ICDD), 1997). With the progress of hydrothermal reaction, the diffraction peaks of $SrTiO_3$ become more and more intense, suggesting the gradual crystallization of $SrTiO_3$. Neither anatase nor rutile diffraction peaks of TiO_2 are observed during the entire hydrothermal process, indicating a direct phase transformation from amorphous TiO_2 hydrates to crystallized $SrTiO_3$. The corresponding morphological evolution can be clearly seen from the TEM images shown in Figure 5 b−g. A smooth surface is present in the pristine D-AHTSS (Figure 5b), which becomes slightly rough after a short hydrothermal reaction (0.5 h) that is ascribed to the formation of $SrTiO_3$ nanocrystallites (Figure 5c). Because of the space confinement, the crystallization merely happens at the surface of nonporous D-AHTSS. The sphere surface becomes much rougher as $SrTiO_3$ grows into larger crystallites and almost covers the entire surface of D-AHTSS after 1.0 h reaction (Figure 5d). Further increasing the reaction time to 2.0 h results in the formation of a core−shell-like structure, with a thin crystallized $SrTiO_3$ shell and a spherical solid core (Figure 5e). The shell becomes thicker when further prolonging the hydrothermal duration to 3.0 h, whereas the core becomes smaller and isolates from the shell, resulting in a yolk−shell structure (Figure 5f). As identified by the XRD analysis, the yolk−shell-structured intermediates show only one $SrTiO_3$ phase; however, anatase phase (PDF no. 21-1272, ICDD, 1969) appears upon calcination (Figure S3), suggesting that the yolk indeed is made of amorphous TiO_2 hydrate, which is intact during hydrothermal process and is crystallized to anatase upon heat treatment. This, together with the perfect spherical structure remaining in the decrescent D-AHTSS, implies that the hollowing process is plausibly induced by an outward Ostwald ripening. This means that along with the inward reaction of D-AHTSS with $Sr(OH)_2$ the high-energy species beneath would presumably relocate onto the $SrTiO_3$ shell via Ostwald ripening. Hence, the shell growth is prompted, and

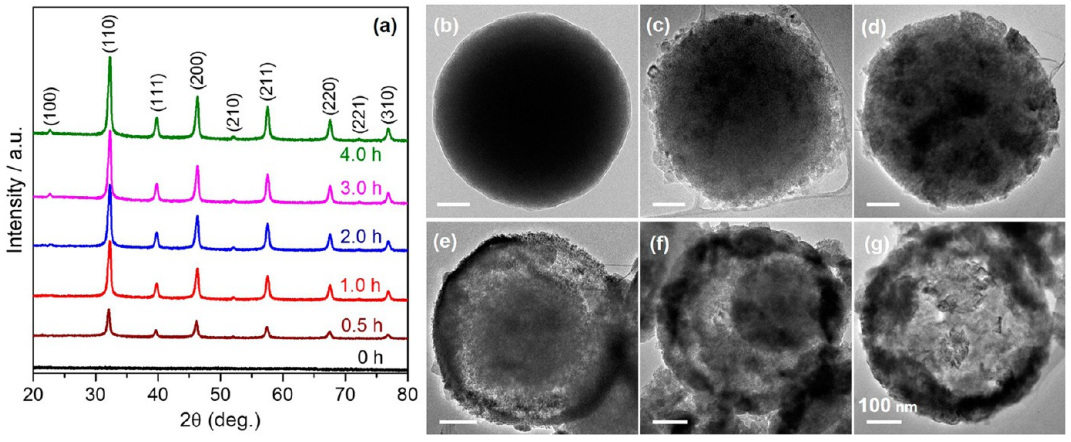

Figure 5. Phase and morphological evolutions from D-AHTSS to $SrTiO_3$ hollow spheres during the hydrothermal process: (a) XRD patterns and TEM images of products obtained with different durations: (b) 0 h, (c) 0.5 h, (d) 1.0 h, (e) 2.0 h, (f) 3.0 h, and (g) 4.0 h.

DOI: 10.1021/acsami.5b03396
ACS Appl. Mater. Interfaces 2015, 7, 14859−14869

voids appear at the TiO_2 hydrate/$SrTiO_3$ interface. Hollow submicrospheres are eventually formed after a 4.0 h reaction when the hydrous TiO_2 species are completely consumed (Figure 5g). Further increases in the hydrothermal reaction time, however, leads to an "over-ripening" of $SrTiO_3$. The spherical morphology gets distorted, and a considerable amount of disassembled free NPs coexists in the final product (Figure S4).

Although the above time-dependent analysis has unambiguously drawn a mesoscopic picture on the formation of hollow submicrospheres, the microscopic picture is yet clear. During the hydrothermal process, the surface of D-AHTSS submicrospheres would gradually transform to the crystallized $SrTiO_3$ phase. It is reasonable to assume that both the Sr^{2+} and OH^- species would further penetrate through the generated mesopores and attack the amorphous TiO_2 hydrate to form $SrTiO_3$ nanocrystallites, which accompanies the expulsion of assembled DDA molecules. The newly formed $SrTiO_3$ nanocrystallites will subsequently undergo Ostwald ripening and redeposit onto the $SrTiO_3$ shell. Alternatively, the newly exposed TiO_2 hydrates underneath the $SrTiO_3$ shell may experience similar Ostwald ripening and form crystalline $SrTiO_3$ on the shell by reacting with $Sr(OH)_2$ in the solution. In either case, core−shell and then yolk−shell intermediate structures of amorphous TiO_2@crystallized $SrTiO_3$ are successively formed before the hollow inner structure is eventually generated in $SrTiO_3$ submicrospheres.

Unlike *h*-$SrTiO_3$, no reconstitution happens during the hydrothermal formation of *s*-$SrTiO_3$, as evidenced by an identical time-dependent morphological analysis (Figure S5). The highly porous structure in N-AHTSS offers good accessibility to the dissolved Sr^{2+} and OH^- species. The inside nanobuilding blocks, hydrous TiO_2, gradually dehydrate, and heterogeneous nucleation of pseudocubelike $SrTiO_3$ nanocrystallites is triggered on the surface of each nanosized TiO_2 hydrate under the mild alkaline condition. The crystallization process does not distort the original spherical morphology. Thus, the formation of $SrTiO_3$ nanocrystallites in this study is believed to involve an in situ crystallization mechanism,[51,60] rather than a dissolution−precipitation mechanism.[42,61] It is noteworthy that both of the above two formation mechanisms have been proposed for the formation of crystalline $SrTiO_3$ although controversy persists because of the difficulty in getting real-time characterizations of the microstructures of intermediates. Our synthesis of porous hierarchical $SrTiO_3$ submicrospheres reported here for the first time offers direct evidence to support the in situ transformation model mesoscopically. The phase transformation from amorphous TiO_2 hydrates to $SrTiO_3$ nanocrystallites leads to a decrease in the surface area of submicrospheres to 170.2 $m^2\ g^{-1}$ after hydrothermal process and an increase in pore size to 6.1 nm (Figure S2).

3.4. Generalization of the Self-Template Strategy. To corroborate the proposed formation mechanism, attempts have been made to extend our synthesis strategy to other $ATiO_3$ submicrospheres, including $CaTiO_3$ and $BaTiO_3$. We selected 400 nm N-AHTSS and 600 nm D-AHTSS as the self-template for the synthesis of porous $CaTiO_3$ solid submicrospheres and $BaTiO_3$ hollow submicrospheres, respectively. Figure 6a shows their XRD patterns that are consistent with PDF nos. 22-0153 and 74-1968 (ICDD, 1971 and 1997), respectively, suggesting that well-crystallized perovskite phases of $CaTiO_3$ and $BaTiO_3$ are obtained. Electron microscopy characterization reveals that

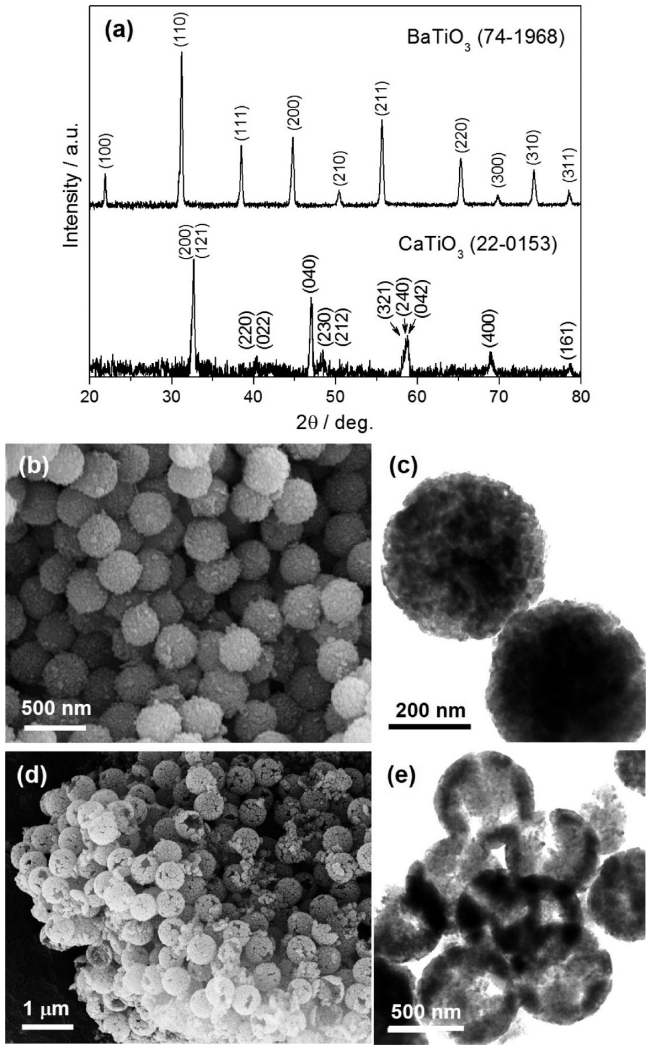

Figure 6. (a) XRD patterns of $CaTiO_3$ solid spheres and $BaTiO_3$ hollow spheres. (b and d) SEM and (c and e) TEM images of porous $CaTiO_3$ solid spheres (b and c) and $BaTiO_3$ hollow spheres (d and e) with average particle sizes of 330 and 560 nm, respectively.

porous $CaTiO_3$ solid submicrospheres with an average diameter of ∼360 nm (Figure 6b,c) and $BaTiO_3$ hollow submicrospheres with an average diameter of ∼570 nm (Figure 6d,e) are successfully synthesized.

The above has shown compelling results that a range of $ATiO_3$ submicrospheres could be feasibly synthesized by a low-temperature hydrothermal process using AHTSS as the template and Ti source. By simply adjusting the properties (particularly, the size and porosity by tuning the SDA and R_H) of AHTSS, this strategy allows for size-controllable synthesis of porous $ATiO_3$ solid or hollow submicrospheres.

3.5. Photocatalytic Activity for O_2 Evolution. The optical characteristics and band gap energies (E_g) of *s*-/*h*-$SrTiO_3$ were studied using diffuse reflectance UV−vis spectroscopy. For comparison, $SrTiO_3$ NPs synthesized by a similar hydrothermal method at 180 °C using P25 TiO_2 as the Ti source were used as reference material. This material has a surface area of 12.6 $m^2\ g^{-1}$ and a particle size of 40−70 nm (Figure S6). Figure 7a shows their UV−visible spectra. All three samples show a significant increase in absorption at wavelengths shorter than 400 nm, which can be assigned to the intrinsic band gap absorption. According to the Kubelka−Munk

DOI: 10.1021/acsami.5b03396
ACS Appl. Mater. Interfaces 2015, 7, 14859−14869

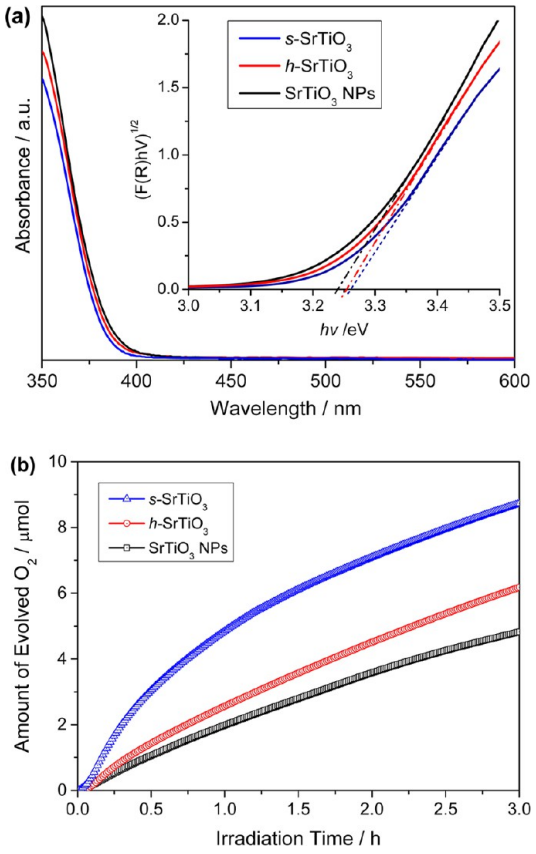

Figure 7. (a) UV−vis diffuse reflectance spectra of $SrTiO_3$ nanoparticles (NPs) and *s*-/*h*-$SrTiO_3$, and (b) their photocatalytic O_2 evolution from 0.05 mol L^{-1} $AgNO_3$ solution. Conditions: 1.0 g L^{-1} $SrTiO_3$, 50 mL of suspensions, and UV illumination using 365 nm LED (light intensity = 44 mW cm^{-2}).

function, E_g for an indirect semiconductor such as $SrTiO_3$ can be estimated by plotting $(F(R_\infty)h\nu)^{1/2}$ versus $h\nu$ (i.e., $1240/\lambda$), where $F(R_\infty) = (1 - R_\infty)^2/2R_\infty$, R_∞ is the reflectance, h is the Planck's constant, ν is the oscillation frequency, and λ is the associated wavelength. The thus-obtained plot is shown in the inset of Figure 7a. By extending a straight line tangential to the slope to cut the horizontal axis, E_g of the *h*-/*s*-$SrTiO_3$ submicrospheres can be estimated to be around 3.25−3.26 eV, comparable to $SrTiO_3$ NPs.

The photocatalytic oxygen evolution measurements were performed in a sealed continuous-flow photoreactor filled with $SrTiO_3$ suspension (1 g L^{-1}) in an $AgNO_3$ (0.01 mol L^{-1}) aqueous solution (50 mL) under 365 nm LED light irradiation (44 mW cm^{-2}). Herein, $AgNO_3$ was used as a sacrificial electron acceptor. The photocatalytic O_2 evolution reactions can be simply described as follows.[62]

$$4h^+ + 2H_2O \rightarrow O_2 \uparrow + 4H^+ \quad (O_2 \text{ evolution reaction}) \tag{1}$$

$$4e^- + 4Ag^+ \rightarrow 4Ag \quad (\text{Ag reduction}) \tag{2}$$

$$nAg \rightarrow Ag_n \quad (\text{growth}) \tag{3}$$

The time profiles of O_2 gas generated over different $SrTiO_3$ materials were monitored by QMS, and the results are shown in Figure 7b. The photocatalytic activity for O_2 evolution of the porous $SrTiO_3$ submicrospheres significantly outperforms that of the $SrTiO_3$ NPs. At the initial stage (t < 0.5 h), gaseous O_2 vigorously evolves. Particularly, *s*-$SrTiO_3$ shows the highest O_2 evolution rate (~7.5 μmol h^{-1}). With increasing reaction time, the O_2 evolution slows down because the formed metallic Ag species on the $SrTiO_3$ surface not only eliminate the active sites but also shield the incident light.[12] After 3.0 h of irradiation time, the total amount of the evolved O_2 is 8.72 and 6.14 μmol for *s*-/*h*-$SrTiO_3$, respectively. In contrast, the photocatalytic activity of the $SrTiO_3$ NPs was found to be notably lower (4.81 μmol O_2) as compared to that of the porous $SrTiO_3$ submicrospheres (Figure 7b). These results clearly indicate the beneficial effect of the large surface area, prompting its interaction with the Ag^+ ions acting as oxidant and thus enabling the photocatalytic generation of O_2. In addition, the superior photocatalytic activity may also partially be attributed to the porous spherical morphology that enables enhanced light harvesting by scattering and reflection[40] as to be shown in the subsequent section.

3.6. Photovoltaic Performance in Mesoscopic Sensitized Solar Cells. A light-scattering layer on top of the nanocrystalline active layer is generally employed in the photoanode of mesoscopic sensitized solar cells to enhance light harnessing. Besides the refractive index, light scattering of a material is largely dependent on its shape and dimension, of which submicrospheres show particular advantages over other morphologies. For instance, the optimal size is ~400−500 nm for the widely used rutile TiO_2 submicroparticles.[4,63] Considering that $SrTiO_3$ has a comparable refractive index (~2.41) and favorable band alignment toward anatase TiO_2,[19] here for the first time we use ternary metal oxide—porous $SrTiO_3$ submicrospheres (~430 nm) as the light-scattering material for semiconductor-sensitized solar cells.

We first investigated the UV−vis spectra of the electrodes. The 3.5 μm thick P25 TiO_2 layer is found to be nearly transparent in the visible region. The transmittance is around 40% at λ = 400 nm (Figure 8a) and gradually increases to 90% at λ > 700 nm. With an additional 3.0 μm thick coating of *s*-/*h*-$SrTiO_3$ submicrospheres, both of the multilayered $SrTiO_3$/TiO_2 films become completely opaque, and their transmittances are almost zero in the wavelength range of 350−800 nm, indicating that the incident light passing through the films is effectively scattered by the porous $SrTiO_3$ submicrospheres. Compared with *s*-$SrTiO_3$, *h*-$SrTiO_3$ shows an even higher reflectance (Figure 8b), plausibly because of their hollow interior enhancing the multiple light scattering. Therefore, the existence of a spherical-$SrTiO_3$-based scattering layer would greatly enhance light harvesting, which prolongs the duration of incident photons traveling within the photoanode and is particularly interesting for mesoscopic solar cells.

CdSe was used as the sensitizer for mesoscopic $SrTiO_3$/TiO_2 solar cells because its absorption spectrum covers most of the visible region. A successive ionic layer adsorption and reaction (SILAR) method was used to deposit the CdSe sensitizer conformally onto the nanocrystalline electrodes.[46] Then, a thin passivation layer of ZnS was deposited onto the sensitized electrodes by the same SILAR method to hinder the backward electron flow from the sensitizer to the oxidized species in the polysulfide electrolyte.[44]

Figure 9a shows the IPCE spectra of CdSe-sensitized mesoscopic solar cells using Pt as the counter electrode. Strong photoresponse is observed over the entire visible light range. Typically, with *s*-/*h*-$SrTiO_3$ as scattering layer, a significantly improved external quantum efficiency in the long wavelength region (λ > 600 nm) is observed, which is mainly ascribed to

DOI: 10.1021/acsami.5b03396
ACS Appl. Mater. Interfaces 2015, 7, 14859−14869

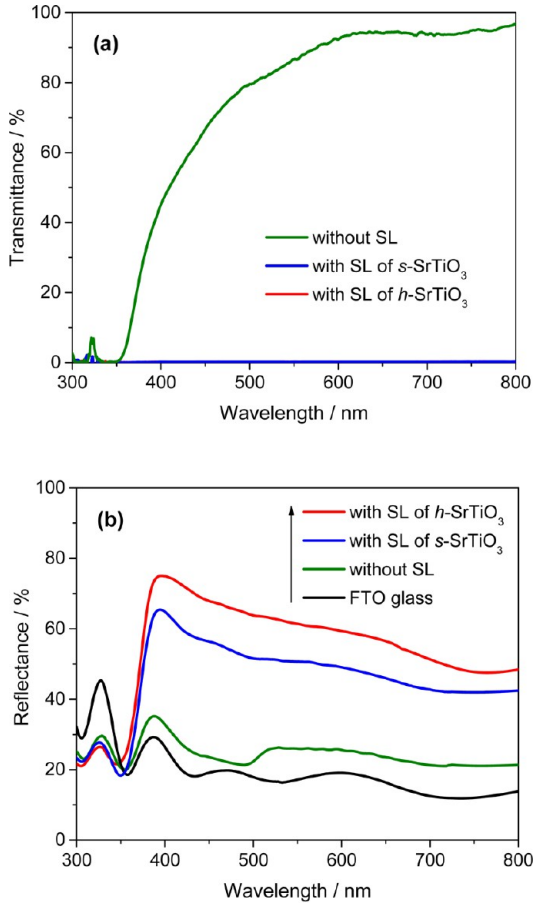

Figure 8. (a) UV−vis transmittance and (b) reflectance spectra of FTO/TiO_2/$SrTiO_3$ photoanodes. The photoanodes consist of a 3.5 μm thick P25 layer with/without a 3.0 μm thick scattering layer (SL) of *s*-/*h*-$SrTiO_3$.

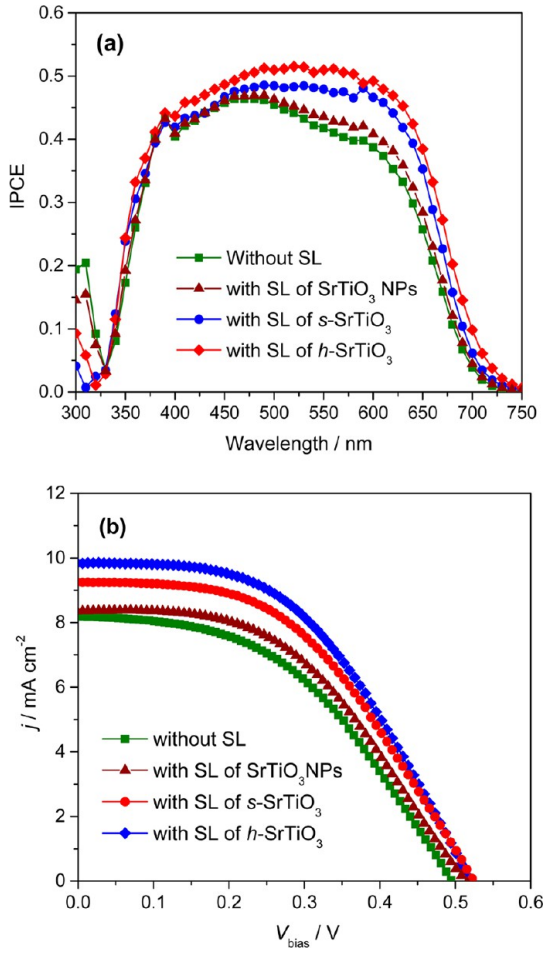

Figure 9. (a) IPCE and (b) *j*−*V* characteristics of CdSe-sensitized solar cells. The photoanodes consist of a 3.5 μm thick P25 transparent layer with/without a 3.0 μm thick scattering layer of *s*-/*h*-$SrTiO_3$ or NPs. Pt and polysulfide were used as the counter electrode and electrolyte, respectively.

the enhanced light scattering by the submicrospherical structures. Decreasing the size of $SrTiO_3$ from submicrometer to dozens of nanometers results in a dramatic drop of light scattering. As can be seen, the incorporation of a light-scattering layer made of $SrTiO_3$ NPs does not remarkably improve the IPCE of the solar cells.

Figure 9b shows the photocurrent−photovoltage (*j*−*V*) characteristics of CdSe-sensitized TiO_2 solar cells with and without $SrTiO_3$ scattering layers. The detailed data are summarized in Table 1. A notable improvement in photovoltage is observed for cells with $SrTiO_3$ scattering layers, which is presumably associated with the formation of a $SrTiO_3$/TiO_2 heterojunction favorable for the charge collection. It is known that $SrTiO_3$ has a similar valence band position as TiO_2 but a higher conduction band edge,[19] considering its E_g of 3.25 eV, which is larger than that of P25 (3.16 eV).[51] The higher V_{oc} is substantiated with the high photovoltage of a cell solely employing a 3 μm thick CdSe-sensitized *h*-$SrTiO_3$ photoanode (Figure S7) despite the extremely low photocurrent.

In addition to the enhanced photovoltage, photoanodes with *s*-/*h*-$SrTiO_3$ scattering layers also revealed augmented photocurrents in *j*−*V* measurement. In contrast, a $SrTiO_3$-NP scattering layer only leads to marginal improvement, which together with the fact that low photocurrent is delivered by $SrTiO_3$ itself (Figure S7) confirms that the enhanced photocurrent is mainly ascribed to the excellent light-scattering properties of *s*-/*h*-$SrTiO_3$.

With *h*-$SrTiO_3$ as the scattering layer, we then optimized the thickness of the TiO_2 layer to 6 μm, which leads to η of 3.82%, comparable to that of the cell made with the rutile TiO_2 scattering layer paste (dye−sol) (η = 3.73%; Figure S8 and Table 1). Furthermore, replacing the Pt counter electrode with Cu_2S renders an impressive η of 5.16% (Figure 10) as a result of drastically enhanced photocurrent,[45,46,48,64] which is among the highest reported efficiencies for CdSe-sensitized solar cells. (The reason is not yet clear why the striking effect of Cu_2S has been observed in several reports.)

4. CONCLUSIONS

A general self-template synthesis strategy combining sol−gel and hydrothermal processes has been developed for the large-scale and size-controllable synthesis of porous $ATiO_3$ solid/hollow submicrospheres. By tuning the size and porosity of AHTSS, spherical $ATiO_3$ (A = Sr, Ba, and Ca) of different size and inner structures could be feasibly synthesized. The underlying formation mechanism of the hollow submicrospheres has been unraveled to involve concomitant surface crystallization and outward Ostwald ripening during the hydrothermal process, whereas solid submicrospheres are formed via an in situ crystallization. The thus-obtained porous $SrTiO_3$ submicrospheres consist of well-organized single-crystal

DOI: 10.1021/acsami.5b03396
ACS Appl. Mater. Interfaces 2015, 7, 14859−14869

Table 1. Characteristics of CdSe-Sensitized TiO_2 Solar Cells with $SrTiO_3$ Scattering Layers under Simulated AM 1.5G, 100 mW cm^{-2} Illumination

photoanode composition	counter electrode	V_{oc} (V)	j_{sc} (mA/cm^2)	*ff* (%)	η (%)[a]
TiO_2 (3.5 + 0)[b]	Pt	0.494	8.15	46.3	1.86 ± 0.05
h-$SrTiO_3$ (0 + 3)[c]	Pt	0.532	2.20	25.8	0.30 ± 0.01
h-$SrTiO_3$ (3.5 + 3)[d]	Pt	0.518	9.82	48.4	2.46 ± 0.07
s-$SrTiO_3$ (3.5 + 3)[e]	Pt	0.522	9.23	47.4	2.28 ± 0.06
$SrTiO_3$ NPs (3.5 + 3)[f]	Pt	0.515	8.34	47.2	2.03 ± 0.08
h-$SrTiO_3$ (6 + 3)[g]	Pt	0.494	13.1	59.2	3.82 ± 0.13
rutile (6 + 3)[h]	Pt	0.483	14.8	52.2	3.73 ± 0.12
h-$SrTiO_3$ (6 + 3)	Cu_2S	0.523	18.5	53.4	5.16 ± 0.17

[a]The standard deviation of the solar cell efficiency was from the data of three devices.[45] [b]Photoanode made of a 3.5 μm thick TiO_2 layer without any scattering layer. [c]Photoanode made of a 3 μm thick *h*-$SrTiO_3$ layer directly used as active layer and without any TiO_2 layer. [d]Photoanode made of a 3.5 μm thick TiO_2 layer and a 3 μm thick scattering layer of *s*-$SrTiO_3$. [e]Photoanode made of a 3.5 μm thick TiO_2 layer and a 3 μm thick scattering layer of *h*-$SrTiO_3$. [f]Photoanode made of a 3.5 μm thick TiO_2 layer and a 3 μm thick scattering layer of $SrTiO_3$ NPs. [g]Photoanode made of a 6 μm thick TiO_2 layer and a 3 μm thick scattering layer of *h*-$SrTiO_3$. [h]Photoanode made of a 6 μm thick TiO_2 layer and a 3 μm thick scattering layer of rutile TiO_2 submicroparticles.

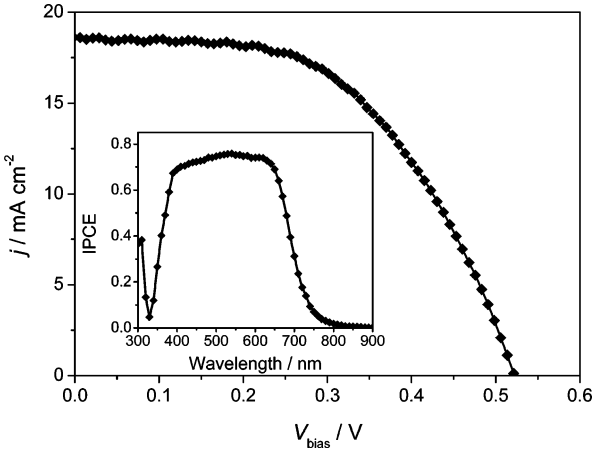

Figure 10. *j*–*V* and IPCE (inset) characteristics of CdSe-sensitized solar cells with a photoanode consisting of a 6 μm thick P25 layer and a 3 μm thick *h*-$SrTiO_3$ scattering layer. The inset shows the IPCE spectrum. Cu_2S and sulfide/polysulfide were used as the counter electrode and electrolyte, respectively.

nanocubes and possess a large specific surface area. These interesting textural properties, integrated with their intrinsic band structure, render superior photocatalytic activity for O_2 evolution and enhanced photocurrent and photovoltage, and thus power conversion efficiency (η) for CdSe-sensitized mesoscopic solar cells. This green and facile synthesis strategy is expected to provide intriguing possibilities for the controllable synthesis of other titanate submicrospheres with desirable structural properties for various applications.

■ ASSOCIATED CONTENT

Supporting Information

XRD, SEM, TEM, *j*–*V*, and IPCE curves of $SrTiO_3$. The Supporting Information is available free of charge on the ACS Publications website at DOI: 10.1021/acsami.5b03396.

■ AUTHOR INFORMATION

Corresponding Author

*E-mail: msewq@nus.edu.sg. Tel.: +65 6516-7118. Fax: +65 6776-3604.

Notes

The authors declare no competing financial interest.

■ ACKNOWLEDGMENTS

Q.W. acknowledges financial support by the National Research Foundation, Prime Minister's Office, Singapore, under its Competitive Research Program (CRP award no. NRF-CRP8-2011-04). I.I. and D.W.B. acknowledge financial support by the BMBF (Bundesministerium für Bildung und Forschung), research project DuaSol (03SF0482C). D.W.B. gratefully acknowledges support by the Project "Establishment of the Laboratory of Photoactive Nanocomposite Materials" (no. 14.Z50.31.0016) supported by a Grant from the Government of the Russian Federation. We thank Dr. Yongliang Zhao and Dr. Gang Han for their help in UV–vis spectroscopy analysis, and Mr. Elisban Sacari for checking ICDD PDF cards.

■ REFERENCES

(1) Schneider, J.; Matsuoka, M.; Takeuchi, M.; Zhang, J.; Horiuchi, Y.; Anpo, M.; Bahnemann, D. W. Understanding TiO_2 Photocatalysis: Mechanisms and Materials. *Chem. Rev.* **2014**, *114* (19), 9919–9986.

(2) Valdes, A.; Brillet, J.; Gratzel, M.; Gudmundsdottir, H.; Hansen, H. A.; Jonsson, H.; Klupfel, P.; Kroes, G.-J.; Le Formal, F.; Man, I. C.; Martins, R. S.; Nørskov, J. K.; Rossmeisl, J.; Sivula, K.; Vojvodic, A.; Zach, M. Solar Hydrogen Production with Semiconductor Metal Oxides: New Directions in Experiment and Theory. *Phys. Chem. Chem. Phys.* **2012**, *14* (1), 49–70.

(3) Chen, H.-Y.; Xu, Y.-F.; Kuang, D.-B.; Su, C.-Y. Recent Advances in Hierarchical Macroporous Composite Structures for Photoelectric Conversion. *Energy Environ. Sci.* **2014**, *7* (12), 3887–3901.

(4) Chen, D.; Caruso, R. A. Recent Progress in the Synthesis of Spherical Titania Nanostructures and Their Applications. *Adv. Funct. Mater.* **2013**, *23* (11), 1356–1374.

(5) Pan, J. H.; Wang, Q.; Bahnemann, D. W. Hydrous TiO_2 Spheres: An Excellent Platform for the Rational Design of Mesoporous Anatase Spheres for Photoelectrochemical Applications. *Catal. Today* **2014**, *230*, 197–204.

(6) Pang, A.; Sun, X.; Ruan, H.; Li, Y.; Dai, S.; Wei, M. Highly Efficient Dye-Sensitized Solar Cells Composed of TiO_2@SnO_2 Core-Shell Microspheres. *Nano Energy* **2014**, *5*, 82–90.

(7) Veerappan, G.; Yu, S.; Wang, D. H.; Lee, W. I.; Park, J. H. Facile Control of Intra- and Inter-Particle Porosity in Template-Free Synthesis of Size-Controlled Nanoporous Titanium Dioxides Beads for Efficient Organic-Inorganic Heterojunction Solar Cells. *J. Power Sources* **2015**, *279*, 72–79.

(8) Hwang, S. H.; Yun, J.; Jang, J. Multi-Shell Porous TiO_2 Hollow Nanoparticles for Enhanced Light Harvesting in Dye-Sensitized Solar Cells. *Adv. Funct. Mater.* **2014**, *24* (48), 7619–7626.

(9) Rawal, S. B.; Kim, H. J.; Lee, W. I. Enhanced Visible-Light Photocatalytic Properties of Fe^{3+}-Grafted N-Doped TiO_2 Nanoporous Spheres. *Appl. Catal., B* **2013**, *142–143*, 458–464.

(10) Cao, L.; Chen, D.; Caruso, R. A. Surface-Metastable Phase-Initiated Seeding and Ostwald Ripening: A Facile Fluorine-Free Process Towards Spherical Fluffy Core/Shell, Yolk/Shell, and Hollow

DOI: 10.1021/acsami.5b03396
ACS Appl. Mater. Interfaces 2015, 7, 14859–14869

Anatase Nanostructures. *Angew. Chem., Int. Ed.* **2013**, *52* (42), 10986−10991.
(11) Royer, S.; Duprez, D.; Can, F.; Courtois, X.; Batiot-Dupeyrat, C.; Laassiri, S.; Alamdari, H. Perovskites as Substitutes of Noble Metals for Heterogeneous Catalysis: Dream or Reality. *Chem. Rev.* **2014**, *114* (20), 10292−10368.
(12) Asai, R.; Nemoto, H.; Jia, Q.; Saito, K.; Iwase, A.; Kudo, A. A Visible Light Responsive Rhodium and Antimony-Codoped $SrTiO_3$ Powdered Photocatalyst Loaded with an IrO_2 Cocatalyst for Solar Water Splitting. *Chem. Commun.* **2014**, *50* (19), 2543−2546.
(13) Pan, C.; Takata, T.; Nakabayashi, M.; Matsumoto, T.; Shibata, N.; Ikuhara, Y.; Domen, K. A Complex Perovskite-Type Oxynitride: The First Photocatalyst for Water Splitting Operable at up to 600 nm. *Angew. Chem., Int. Ed.* **2015**, *54* (10), 2955−2959.
(14) Abutaha, A. I.; Kumar, S. R. S.; Li, K.; Dehkordi, A. M.; Tritt, T. M.; Alshareef, H. N. Enhanced Thermoelectric Figure-of-Merit in Thermally Robust, Nanostructured Superlattices Based on $SrTiO_3$. *Chem. Mater.* **2015**, *27* (6), 2165−2171.
(15) Domen, K.; Naito, S.; Soma, M.; Onishi, T.; Tamaru, K. Photocatalytic Decomposition of Water Vapour on an NiO-$SrTiO_3$ Catalyst. *J. Chem. Soc., Chem. Commun.* **1980**, *12*, 543−544.
(16) Ouyang, S.; Tong, H.; Umezawa, N.; Cao, J.; Li, P.; Bi, Y.; Zhang, Y.; Ye, J. Surface-Alkalinization-Induced Enhancement of Photocatalytic H_2 Evolution over $SrTiO_3$-Based Photocatalysts. *J. Am. Chem. Soc.* **2012**, *134* (4), 1974−1977.
(17) Kim, C. W.; Suh, S. P.; Choi, M. J.; Kang, Y. S.; Kang, Y. S. Fabrication of $SrTiO_3$-TiO_2 Heterojunction Photoanode with Enlarged Pore Diameter for Dye-Sensitized Solar Cells. *J. Mater. Chem. A* **2013**, *1* (38), 11820−11827.
(18) Diamant, Y.; Chen, S. G.; Melamed, O.; Zaban, A. Core−Shell Nanoporous Electrode for Dye Sensitized Solar Cells: The Effect of the $SrTiO_3$ Shell on the Electronic Properties of the TiO_2 Core. *J. Phys. Chem. B* **2003**, *107* (9), 1977−1981.
(19) Lenzmann, F.; Krueger, J.; Burnside, S.; Brooks, K.; Grätzel, M.; Gal, D.; Rühle, S.; Cahen, D. Surface Photovoltage Spectroscopy of Dye-Sensitized Solar Cells with TiO_2, Nb_2O_5, and $SrTiO_3$ Nanocrystalline Photoanodes: Indication for Electron Injection from Higher Excited Dye States. *J. Phys. Chem. B* **2001**, *105* (27), 6347−6352.
(20) Zhang, H.; Chen, G.; Bahnemann, D. W. Photoelectrocatalytic Materials for Environmental Applications. *J. Mater. Chem.* **2009**, *19* (29), 5089−5121.
(21) Jia, Q.; Iwase, A.; Kudo, A. $BiVO_4$-Ru/$SrTiO_3$:Rh Composite Z-Scheme Photocatalyst for Solar Water Splitting. *Chem. Sci.* **2014**, *5* (4), 1513−1519.
(22) Townsend, T. K.; Browning, N. D.; Osterloh, F. E. Nanoscale Strontium Titanate Photocatalysts for Overall Water Splitting. *ACS Nano* **2012**, *6* (8), 7420−7426.
(23) Niederberger, M.; Pinna, N.; Polleux, J.; Antonietti, M. A General Soft-Chemistry Route to Perovskites and Related Materials: Synthesis of $BaTiO_3$, $BaZrO_3$, and $LiNbO_3$ Nanoparticles. *Angew. Chem., Int. Ed.* **2004**, *43* (17), 2270−2273.
(24) Niederberger, M.; Garnweitner, G.; Pinna, N.; Antonietti, M. Nonaqueous and Halide-Free Route to Crystalline $BaTiO_3$, $SrTiO_3$, and (Ba,Sr)TiO_3 Nanoparticles via a Mechanism Involving C−C Bond Formation. *J. Am. Chem. Soc.* **2004**, *126* (29), 9120−9126.
(25) Zhu, X.; Wang, J.; Zhang, Z.; Zhu, J.; Zhou, S.; Liu, Z.; Ming, N. Perovskite Nanoparticles and Nanowires: Microwave−Hydrothermal Synthesis and Structural Characterization by High-Resolution Transmission Electron Microscopy. *J. Am. Ceram. Soc.* **2008**, *91* (8), 2683−2689.
(26) Xie, K.; Umezawa, N.; Zhang, N.; Reunchan, P.; Zhang, Y.; Ye, J. Self-Doped $Srtio_{3-\delta}$ Photocatalyst with Enhanced Activity for Artificial Photosynthesis under Visible Light. *Energy Environ. Sci.* **2011**, *4* (10), 4211−4219.
(27) Zou, F.; Jiang, Z.; Qin, X.; Zhao, Y.; Jiang, L.; Zhi, J.; Xiao, T.; Edwards, P. P. Template-Free Synthesis of Mesoporous N-Doped $SrTiO_3$ Perovskite with High Visible-Light-Driven Photocatalytic Activity. *Chem. Commun.* **2012**, *48* (68), 8514−8516.
(28) Demirörs, A. F.; Imhof, A. $BaTiO_3$, $SrTiO_3$, $CaTiO_3$, and $Ba_xSr_{1-x}TiO_3$ Particles: A General Approach for Monodisperse Colloidal Perovskites. *Chem. Mater.* **2009**, *21* (13), 3002−3007.
(29) Dong, W.; Li, X.; Yu, J.; Guo, W.; Li, B.; Tan, L.; Li, C.; Shi, J.; Wang, G. Porous $SrTiO_3$ Spheres with Enhanced Photocatalytic Performance. *Mater. Lett.* **2012**, *67* (1), 131−134.
(30) Karakaya, C.; Türker, Y.; Dag, Ö. Molten-Salt-Assisted Self-Assembly (MASA)-Synthesis of Mesoporous Metal Titanate-Titania, Metal Sulfide-Titania, and Metal Selenide-Titania Thin Films. *Adv. Funct. Mater.* **2013**, *23* (32), 4002−4010.
(31) Yang, J.; Geng, B.; Ye, Y.; Yu, X. Stick-Like Titania Precursor Route to $MTiO_3$ (M = Sr, Ba, and Ca) Polyhedra. *CrystEngComm* **2012**, *14* (8), 2959−2965.
(32) Zhang, J.; Bang, J. H.; Tang, C.; Kamat, P. V. Tailored TiO_2-$SrTiO_3$ Heterostructure Nanotube Arrays for Improved Photoelectrochemical Performance. *ACS Nano* **2010**, *4* (1), 387−395.
(33) Zheng, Z.; Huang, B.; Qin, X.; Zhang, X.; Dai, Y. Facile Synthesis of $SrTiO_3$ Hollow Microspheres Built as Assembly of Nanocubes and Their Associated Photocatalytic Activity. *J. Colloid Interface Sci.* **2011**, *358* (1), 68−72.
(34) Mao, Y.; Kanungo, M.; Hemraj-Benny, T.; Wong, S. S. Synthesis and Growth Mechanism of Titanate and Titania One-Dimensional Nanostructures Self-Assembled into Hollow Micrometer-Scale Spherical Aggregates. *J. Phys. Chem. B* **2006**, *110* (2), 702−710.
(35) Pan, J. H.; Dou, H.; Xiong, Z.; Xu, C.; Ma, J.; Zhao, X. S. Porous Photocatalysts for Advanced Water Purifications. *J. Mater. Chem.* **2010**, *20* (22), 4512−4528.
(36) Li, J.; Hietala, S.; Tian, X. $BaTiO_3$ Supercages: Unusual Oriented Nanoparticle Aggregation and Continuous Ordering Transition in Morphology. *ACS Nano* **2015**, *9* (1), 496−502.
(37) Zhang, Y.; Lin, S.; Zhang, W.; Ge, H.; Li, G.; Zhang, Y.; Qi, F.-Y.; Song, X.-M. Synthesis of a Tailored $SrTiO_3$-TiO_3 Microspherical Photocatalyst and Its Photogenerated Charge Properties. *RSC Adv.* **2014**, *4* (7), 3226−3232.
(38) Pan, J. H.; Wang, X. Z.; Huang, Q.; Shen, C.; Koh, Z. Y.; Wang, Q.; Engel, A.; Bahnemann, D. W. Large-Scale Synthesis of Urchin-Like Mesoporous TiO_2 Hollow Spheres by Targeted Etching and Their Photoelectrochemical Properties. *Adv. Funct. Mater.* **2014**, *24* (1), 95−104.
(39) Pan, J. H.; Bai, Y.; Wang, Q. Reconstruction of Colloidal Spheres by Targeted Etching: A Generalized Self-Template Route to Porous Amphoteric Metal Oxide Hollow Spheres. *Langmuir* **2015**, *31* (15), 4566−4572.
(40) Pan, J. H.; Zhang, X.; Du, A. J.; Sun, D. D.; Leckie, J. O. Self-Etching Reconstruction of Hierarchically Mesoporous F-TiO_2 Hollow Microspherical Photocatalyst for Concurrent Membrane Water Purifications. *J. Am. Chem. Soc.* **2008**, *130* (34), 11256−11257.
(41) Pan, J. H.; Han, G.; Zhou, R.; Zhao, X. S. Hierarchical N-Doped TiO_2 Hollow Microspheres Consisting of Nanothorns with Exposed Anatase {101} Facets. *Chem. Commun.* **2011**, *47* (24), 6942−6944.
(42) Walton, R. I.; Millange, F.; Smith, R. I.; Hansen, T. C.; O'Hare, D. Real Time Observation of the Hydrothermal Crystallization of Barium Titanate Using in Situ Neutron Powder Diffraction. *J. Am. Chem. Soc.* **2001**, *123* (50), 12547−12555.
(43) Kandiel, T. A.; Ivanova, I.; Bahnemann, D. W. Long-Term Investigation of the Photocatalytic Hydrogen Production on Platinized TiO_2: An Isotopic Study. *Energy Environ. Sci.* **2014**, *7* (4), 1420−1425.
(44) Hossain, M. A.; Jennings, J. R.; Koh, Z. Y.; Wang, Q. Carrier Generation and Collection in CdS/CdSe-Sensitized SnO_2 Solar Cells Exhibiting Unprecedented Photocurrent Densities. *ACS Nano* **2011**, *5* (4), 3172−3181.
(45) Hossain, M. A.; Jennings, J. R.; Shen, C.; Pan, J. H.; Koh, Z. Y.; Mathews, N.; Wang, Q. Cdse-Sensitized Mesoscopic TiO_2 Solar Cells Exhibiting >5% Efficiency: Redundancy of Cds Buffer Layer. *J. Mater. Chem.* **2012**, *22* (32), 16235−16242.
(46) Shen, C.; Sun, L.; Koh, Z. Y.; Wang, Q. Cuprous Sulfide Counter Electrodes Prepared by Ion Exchange for High-Efficiency Quantum Dot-Sensitized Solar Cells. *J. Mater. Chem. A* **2014**, *2* (8), 2807−2813.

DOI: 10.1021/acsami.5b03396
ACS Appl. Mater. Interfaces 2015, 7, 14859−14869

(47) Shen, C.; Wang, X.; Jiang, X.-F.; Zhu, H.; Li, F.; Yang, J.; Xu, Q.-H.; Wang, Q. Fast Charge Separation at Semiconductor Sensitizer−Molecular Relay Interface Leads to Significantly Enhanced Solar Cell Performance. *J. Phys. Chem. C* **2015**, *119* (18), 9774−9781.
(48) Lee, H.; Wang, M.; Chen, P.; Gamelin, D. R.; Zakeeruddin, S. M.; Grätzel, M.; Nazeeruddin, M. K. Efficient Cdse Quantum Dot-Sensitized Solar Cells Prepared by an Improved Successive Ionic Layer Adsorption and Reaction Process. *Nano Lett.* **2009**, *9* (12), 4221−4227.
(49) Sugimoto, T.; Kojima, T. Formation Mechanism of Amorphous TiO_2 Spheres in Organic Solvents. 1. Roles of Ammonia. *J. Phys. Chem. C* **2008**, *112* (48), 18760−18771.
(50) Pauly, T. R.; Pinnavaia, T. J. Pore Size Modification of Mesoporous Hms Molecular Sieve Silicas with Wormhole Framework Structures. *Chem. Mater.* **2001**, *13* (3), 987−993.
(51) Pan, J. H.; Cai, Z.; Yu, Y.; Zhao, X. S. Controllable Synthesis of Mesoporous F-TiO_2 Spheres for Effective Photocatalysis. *J. Mater. Chem.* **2011**, *21* (30), 11430−11438.
(52) Chen, D.; Cao, L.; Huang, F.; Imperia, P.; Cheng, Y. B.; Caruso, R. A. Synthesis of Monodisperse Mesoporous Titania Beads with Controllable Diameter, High Surface Areas, and Variable Pore Diameters (14−23 nm). *J. Am. Chem. Soc.* **2010**, *132* (12), 4438−4444.
(53) Soler-Illia, G. J. d. A. A.; Sanchez, C.; Lebeau, B.; Patarin, J. Chemical Strategies to Design Textured Materials: From Microporous and Mesoporous Oxides to Nanonetworks and Hierarchical Structures. *Chem. Rev.* **2002**, *102* (11), 4093−4138.
(54) Hong, M. P.; Kim, J. Y.; Vemula, K.; Kim, H. S.; Yoon, K. B. Synthesis of Monodisperse Mesoporous TiO_2 Spheres with Tunable Sizes between 0.6 and 3.1 μm and Effects of Reaction Temperature, Ti Source Purity, and Type of Alkylamine on Size and Monodispersity. *Chem. Commun.* **2012**, *48* (35), 4250−4252.
(55) Hu, L.; Wang, C.; Kennedy, R. M.; Marks, L. D.; Poeppelmeier, K. R. The Role of Oleic Acid: From Synthesis to Assembly of Perovskite Nanocuboid Two-Dimensional Arrays. *Inorg. Chem.* **2015**, *54* (3), 740−745.
(56) Sing, K. S. W.; Everett, D. H.; Haul, R. A. W.; Moscou, L.; Pierotti, R. A.; Rouquerol, J.; Siemieniewska, T. Reporting Physisorption Data for Gas/Solid Systems with Special Reference to the Determination of Surface Area and Porosity (Recommendations 1984). *Pure Appl. Chem.* **1985**, *57* (4), 603−619.
(57) Wang, S.; Ding, Y.; Xu, S.; Zhang, Y.; Li, G.; Hu, L.; Dai, S. TiO_2 Nanospheres: A Facile Size-Tunable Synthesis and Effective Light-Harvesting Layer for Dye-Sensitized Solar Cells. *Chem. - Eur. J.* **2014**, *20* (17), 4916−4920.
(58) Yu, J.; Yu, J. C.; Leung, M. K. P.; Ho, W.; Cheng, B.; Zhao, X.; Zhao, J. Effects of Acidic and Basic Hydrolysis Catalysts on the Photocatalytic Activity and Microstructures of Bimodal Mesoporous Titania. *J. Catal.* **2003**, *217* (1), 69−78.
(59) Kato, H.; Kudo, A. Visible-Light-Response and Photocatalytic Activities of TiO_2 and $SrTiO_3$ Photocatalysts Codoped with Antimony and Chromium. *J. Phys. Chem. B* **2002**, *106* (19), 5029−5034.
(60) Maxim, F.; Ferreira, P.; Vilarinho, P. M.; Reaney, I. Hydrothermal Synthesis and Crystal Growth Studies of $BaTiO_3$ Using Ti Nanotube Precursors. *Cryst. Growth Des.* **2008**, *8* (9), 3309−3315.
(61) Moreira, M. L.; Longo, V. M.; Avansi, W.; Ferrer, M. M.; Andrés, J.; Mastelaro, V. R.; Varela, J. A.; Longo, É. Quantum Mechanics Insight into the Microwave Nucleation of $SrTiO_3$ Nanospheres. *J. Phys. Chem. C* **2012**, *116* (46), 24792−24808.
(62) Schneider, J.; Bahnemann, D. W. Undesired Role of Sacrificial Reagents in Photocatalysis. *J. Phys. Chem. Lett.* **2013**, *4* (20), 3479−3483.
(63) Yu, I. G.; Kim, Y. J.; Kim, H. J.; Lee, C.; Lee, W. I. Size-Dependent Light-Scattering Effects of Nanoporous TiO_2 Spheres in Dye-Sensitized Solar Cells. *J. Mater. Chem.* **2011**, *21* (2), 532−538.
(64) Mora-Seró, I.; Bisquert, J. Breakthroughs in the Development of Semiconductor-Sensitized Solar Cells. *J. Phys. Chem. Lett.* **2010**, *1* (20), 3046−3052.

DOI: 10.1021/acsami.5b03396
ACS Appl. Mater. Interfaces 2015, 7, 14859−14869